

# Coregistered photoacoustic and ultrasonic signatures of early bone density variations

Bahman Lashkari\* and Andreas Mandelis

University of Toronto, Center for Advanced Diffusion-Wave Technologies, Department of Mechanical and Industrial Engineering, 5 King's College Road, Toronto, Ontario M5S 3G8, Canada

**Abstract.** This study examines the application of backscattered ultrasound (US) and photoacoustic (PA) signals for assessment of bone structure and density variations. Both methods were applied in the frequency-domain, employing linear frequency modulation chirps. A near-IR laser (800 nm) was used for inducing the PA signal. The backscattered pressure waves were detected with a 2.2-MHz US transducer. Experiments were focused on detection and evaluation of PA and US signals from *in-vitro* animal and human bones with cortical and trabecular sublayers. It was shown that PA signals can be detected as deep as a few millimeters below trabecular and cortical layers. The occurrence of multiple scattering was demonstrated in PA detected signals from cancellous bone. Osteoporotic changes in the bone were simulated by using a very mild demineralization ethylenediaminetetraacetic acid solution. Changes in the time-domain signals as well as integrated backscattering spectra were compared for the samples before and after demineralization. The results demonstrated the sensitivity of PA to variations in bone minerals. In comparison to PA, US was capable of generating detectable signals from deeper bone sublayers (few centimeters). However, while US signal variations with changes in the cortical layer were insignificant, PA proved to be sensitive even to minor variations of the cortical bone density. © 2014 Society of Photo-Optical Instrumentation Engineers (SPIE) [DOI: 10.1117/1.JBO.19.3.036015]

Keywords: osteoporosis; ultrasonic backscatter; photoacoustics; quantitative ultrasound; cancellous bone; cortical bone.

Paper 130535PRR received Jul. 27, 2013; revised manuscript received Dec. 17, 2013; accepted for publication Feb. 17, 2014; published online Mar. 19, 2014.

## 1 Introduction

Osteoporosis is a disease characterized by a decrease in bone mass and microstructural deterioration of bone tissue, leading to increased risk of fracture.<sup>1</sup> Over the past two decades, osteoporosis has been recognized among the most serious public health problems. Surveys reveal that one in two to three women and one in four to five men over the age of 50 are affected by osteoporosis-related fractures.<sup>2,3</sup> The aforementioned probability for women is much higher than the chance of suffering from breast cancer or cardiovascular disease.<sup>4</sup> The healthcare costs for osteoporotic fractures are billions of dollars annually, and are expected to increase in future. For instance, the cost for the United States is predicted to be between \$30 and \$40 billion by the year 2020 (Ref. 4). Various studies in European countries show similarly large costs of osteoporosis per annum, and the costs and number of patients are increasing due to the growing average population age.<sup>3</sup> Studies in Canada reveal large numbers of patients and healthcare costs as well; for instance, the healthcare cost for male osteoporosis patients over the age of 50 alone is consuming 0.3% of the entire country's healthcare expenditure.<sup>5</sup>

Fortunately, with the growing awareness of osteoporosis, new treatments have been developed for the prevention of fracture.<sup>1</sup> At the same time, there has been a rapid improvement in diagnostic methods.<sup>6</sup> The therapeutic strategies involve pharmacological, dietary and life-style changes. Research in this area is in progress and largely depends on better understanding of the cellular biology and biomechanical structure of the bone.

The available diagnostic methods use various technologies for the noninvasive assessment of bone integrity. Nowadays, the most widely applied method is dual-energy x-ray absorptiometry (DXA or DEXA).<sup>2,6</sup> This method has been established as a reliable means of bone density measurement, but is not able to assess other important aspects like strength and microstructure changes. Another promising technique for noninvasive, cost-effective and safe diagnosis, and screening of osteoporosis is quantitative ultrasound (QUS).<sup>4,7,8</sup> The QUS is conventionally based on the measurement of two key parameters; the speed of sound (SOS) and broadband ultrasonic attenuation (BUA). The strong correlation of SOS and slope of frequency dependent normalized broadband ultrasound attenuation (nBUA) with bone mineral density (BMD) has been confirmed in various reports<sup>4</sup> and several clinical instruments have been developed based on these factors.<sup>7,8</sup> Clinical assessment and issues of QUS compared with the well-established DXA assessment require improvement in devices and protocols associated with QUS.<sup>9</sup>

Although QUS has been mostly focused on nBUA and SOS measurement, there are other ultrasonic methods such as backscattering and fast-slow wave detection which can be used for bone strength evaluation.<sup>4,10</sup> With the exception of ultrasound (US) backscatter, the other mentioned methods depend on through transmission in the cancellous bone and therefore they are limited to specific skeleton sites like the heel (calcaneus). It is known that some skeletal locations are more sensitive to osteoporosis. The backscatter technique provides the possibility of analysis of osteoporosis at sites like the hip or spine, which are otherwise inaccessible for transmission monitoring. In

\*Address all correspondence to: Bahman Lashkari, E-mail: [bahman@mie.utoronto.ca](mailto:bahman@mie.utoronto.ca)

addition, backscatter has demonstrated a close correlation with bone microstructure.<sup>11,12</sup> The main challenge of QUS is the complexity of trabecular bone structure and the large number of unknown parameters in the analysis of ultrasonic wave propagation through this medium, as well as large variation of properties of bones. It should be mentioned that the study of bone backscatter, in addition providing information about bone structure, can lead to a better understanding of US transmission through the bone, specifically the relative roles of absorption and scattering in the acoustic attenuation.<sup>13</sup>

Many parameters have been introduced and examined in US backscatter studies. The frequency-dependent backscatter coefficient [BSC or  $\eta(f)$ ] is among the most important parameters.<sup>14–18</sup> It can be defined as

$$\text{BSC}(f) = \frac{P_{\text{BS}}/P_{\text{ref}}}{\Omega \cdot D} F(f), \quad (1)$$

where  $P_{\text{BS}}$  is the ensemble average of the backscattered power spectrum from the sample, and  $P_{\text{ref}}$  is the backscattered power spectrum from a reference sample.  $\Omega$  is the solid angle generated by the transducer focal zone,  $D$  is the length of time-gated signal in the sample, and  $F(f)$  is a function compensating for attenuation. The frequency dependence of the BSC is studied using simplified models and can be predicted for trabecular bone media.<sup>10,19,20</sup> Although BSC is a frequency dependent parameter that can be measured at a specific frequency (transducer center frequency) or over a frequency range, other backscatter parameters are introduced, which are averaged over a frequency range. This helps quantify the bone pulse-echo response by means of one parameter. One such parameter is the integrated reflection coefficient (IRC),<sup>21–23</sup> which yields the frequency-averaged spectral power of the reflection signal by time-gating the reflected wave. Another parameter is based on the backscatter signal by filtering the directly reflected component of the signal through time gating. This parameter is called the apparent-integrated backscatter (AIB).<sup>13,22–25</sup> These two parameters are defined as

$$\text{IRC or AIB} = \frac{1}{\Delta f} \int_{\Delta f} 20 \log_{10} \left( \frac{S_r}{S_{\text{ref}}} \right) df, \quad (2)$$

where  $S_r$  is the amplitude spectrum of the time-gated signal and it denotes reflected or backscattered signal corresponding to IRC or AIB, respectively,  $S_{\text{ref}}$  is the amplitude spectrum from the reference sample (a perfect reflector), and  $\Delta f$  is the frequency bandwidth of the transducer. Compensating for attenuation inside the trabecular layer, yet another parameter called the broadband ultrasound backscatter (BUB) has been introduced.<sup>12,21,26,27</sup> This is the most prevalent parameter representing the backscatter in trabecular bones while an appropriate method for compensation of attenuation has been discussed vastly in the literature.<sup>10</sup> Other parameters have also been introduced to represent the backscatter from trabecular bones; the frequency slope of the apparent backscatter,<sup>13</sup> the time slope of the apparent backscatter, and the spectral centroid shift<sup>28</sup> are among them.

The aforementioned backscatter parameters exhibit moderate to high correlation not only with the bone volume fraction (BV/TV) but also with the ultimate strength (yield stress), collagen content, trabeculae thickness, and trabeculae separation (TrSp) of bone.<sup>11,12,21,22,23,27</sup> Therefore, backscatter US

represents the structure and composition of bone far more than BMD. The application of simplistic models such as the weak scattering model, Faran's cylinder model and the binary mixture model also supports the frequency dependent relation between backscatter signal and trabeculae size, shape, elasticity, and volume fraction.<sup>10,29</sup> Here, we can conclude that representing bone strength with only one parameter like BMD and attempting to diagnose osteoporosis by measuring only one parameter like BUA could be one of the reasons that clinical QUS has only had modest success. The frequency dependence of ultrasonic parameters forces the indicator parameters to be defined in specific frequencies or to perform frequency averaging. On the other hand, it is possible to take advantage of the variation of parameters with frequency to reduce the error induced by soft tissue overlayers in clinical applications. Dual frequency ultrasound has proven effective in minimizing the effect of soft tissue overlayers.<sup>30,31</sup>

In addition to the assessment of trabecular bone, US has also been applied *in vitro* to cortical bone characterization, where the thickness of the bone in relation to the wavelength defines the mode of wave propagation.<sup>32</sup>

This study shows that by adding photoacoustics (PA) to US, we can garner valuable complementary information about bone composition and structure. PA has been employed before in spectroscopy mode to bone healing assessment of fractured rat bone (*in-vitro*).<sup>33</sup> In another study, PA was used for imaging teeth to identify demineralization diseases such as carious decay.<sup>34</sup> *In-vitro* PA tomography and *in-vivo* dual-mode PA and US imaging of finger joints for diagnosis of inflammatory arthritis has also been reported.<sup>35,36</sup> These imaging tasks were focused on blood as the main chromophore and very few details were given on the phalanx structure. Our group introduced PA diagnostics for studies of bone density changes. In our previous work,<sup>37</sup> we showed that the PA signal is sensitive to large changes in the trabecular bone structure. We also showed that “coherent structure backscattering” similar to US<sup>38</sup> can be detected with PA at frequencies higher than 1 MHz. Another means of employing PA on bone is in excitation of ultrasonic-guided waves.<sup>39,40</sup>

In this study, we applied coregistered frequency-domain (FD) US and PA to bone studies. It should be mentioned that FD-US has been previously applied in QUS in the measurement of BUA,<sup>41,42</sup> detection of fast-slow waves<sup>43</sup> and guided waves in long bones.<sup>44</sup> Application of combined FD-US and PA not only helps enhance SNR as compared with time-domain PA and US but also is an optimal method for spectral studies of the signal due to the deterministic transmission spectrum. Our method is based on comparison between the PA and US signals of trabecular bones before and after artificial demineralization steps. We employed the experiments in a way to make sure that the measurements were performed at the same points before and after demineralization. It should be added that there is a large challenge to extend the findings presented in this article, particularly in the PA modality, to *in-vivo* experiments where the presence of blood, lipids, and skin overlayer may interfere. There are possible solutions to overcome this complication. Similar to the US modality, employing dual frequency can minimize the effect of soft tissue. In addition, PA has the potential to be used in multi-wavelength detection with different sensitivities to blood, lipids, and hydroxyapatite. The other suggestion is employing the method probing the cortical layer in skeletal sites with minimum tissue overlayer.

## 2 Materials and Methods

### 2.1 Coded Excitation PA and US Imaging

The use of coded excitation signals in US imaging and its benefits are discussed elsewhere.<sup>45</sup> The appropriate method for our application is the use of a linear frequency modulation signal, which generates high-SNR enhancement and linear frequency spectrum in the selected range. The instantaneous frequency is defined as

$$f(t) = f_c + \left(\frac{B_{ch}}{T}\right)t, \quad (3)$$

where  $f_c$  is the chirp center frequency,  $B_{ch}$  is the frequency bandwidth of the chirp, and  $T$  is the chirp duration ( $-\frac{1}{2}T < t < \frac{1}{2}T$ ). The matched filter signal, which is the cross-correlation of the transmitted and detected signals yields the delay time ( $\tau$ ) of the scatterers as

$$R(\tau) = T \frac{\sin[\pi B_{ch}\tau(1 - \tau/T)]}{\pi B_{ch}\tau} e^{j2\pi f_c \tau}. \quad (4)$$

Other factors such as acoustic attenuation and transducer transfer function affect the sinc-function shape of the US signal. In addition to these factors, the energy conversion process in PA tends to dominate the signal shape.<sup>46</sup> By employing reference signals from a perfect reflector in US and a homogeneous known absorber in PA, the effects of transducer and instrumentation can be compensated for. Here, spectral analysis is the main goal and therefore a suitable frequency range should be selected to optimize the response depending on the average size of the scatterers. A middle stage in the spectral analysis is the time-gating of the time-domain cross-correlation signal and transforming back into FD. Time-gating provides the facility to separate the various parts of the signal generated by direct reflection from cortical and other overlayers and through backscattering from the trabecular layer.

### 2.2 Combined PA and US Coregistration Experimental Set-up

The experimental set-up is depicted in Fig. 1(a). This set-up facilitates separate PA and US tests at the same coordinate location of bone samples. Optical excitation of the PA probe was

generated using a CW 800-nm diode-laser (Jenoptik AG, Jena, Germany). The laser driver was controlled by a software function generator to modulate the laser intensity. A collimator was used to generate a collimated laser beam with 2-mm spotsize on the sample. The choice of 800 nm was made for maximum penetration depth in bone tissue in the near-IR region.<sup>47</sup> A 3.5-MHz focused ultrasonic transducer was used for transmitting the US signal (V382, Olympus NDT Inc., Panametrics, Waltham, Massachusetts). This transducer has 0.5 in. element size and 1 in. focal length. Beam width at half maximum was estimated to be 0.87 mm.<sup>48</sup> The sensitivity of this transducer was measured with a calibrated hydrophone and was found to be  $31.8 \mu\text{V}/\text{Pa}$ .<sup>49</sup> By employing the reciprocity property of piezoceramics, we could estimate the transmitted US intensity generated by this transducer. The RMS US amplitude was 2.25 mV. This signal was 40 dB amplified by the RF power amplifier (411LA ENI Co., Rochester, New York, 10 W) connected with the transducer which thus generated a pressure of 72 kPa at the focal zone or  $34,800 \text{ kW}/\text{cm}^2$  in water.

Backscattered pressure waves were detected with a 2.2-MHz focused transducer (V305, Olympus NDT Inc., Panametrics, Waltham, Massachusetts) of 0.75 in. diameter and 1 in. focal length. The beamwidth was estimated to be 0.9 mm.<sup>48</sup> Different transducers are employed to provide the possibility of testing a wider range of frequencies by switching the transducers, however, in this report, the 2.2-MHz transducer was used as receiver and the 3.5-MHz transducer was used as transmitter. Both transducers provide good sensitivity in the selected frequency range of the chirps and the effect of transducer and instrumentation has been compensated by normalizing with reference US and PA spectra as explained further on.

The bone sample and the transducer were located in a water container for acoustic coupling. The system was designed for back propagating detection and there was a  $\sim 27^\circ$  deg angle between the laser beam and each transducer's center line. The point of incidence of the laser beam was perpendicular to the water surface. The laser beam was further used to adjust the focal point of both transducers on the same spot on the sample. The US focal beam widths of both transducers were very close and  $< 1 \text{ mm}$ . In the experiments, we used stepsizes  $\geq 1 \text{ mm}$  between the measured A-scans to prevent overlapping between measurements. According to the literature  $< 50\%$  cross-sectional overlap between regions of interest is required to ensure independent data.<sup>29</sup>

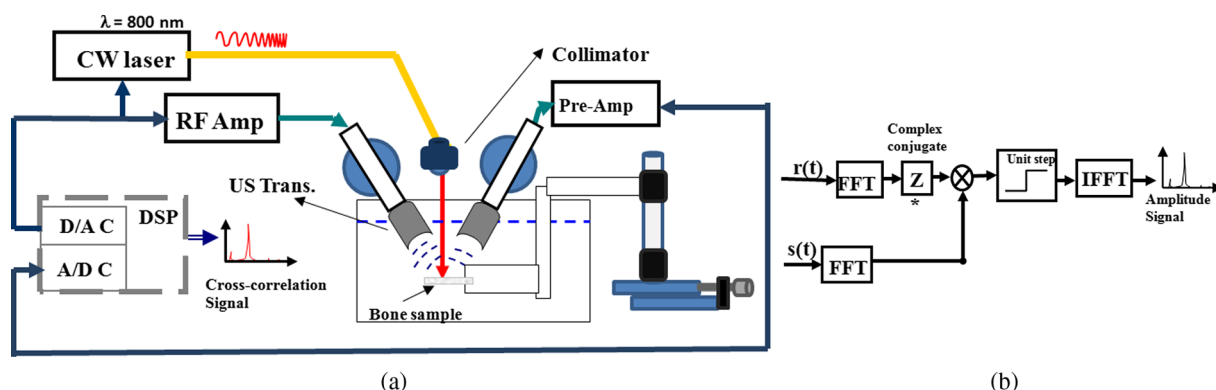


**Fig. 1** (a) Block diagram of combined (“coregistration”) photoacoustic (PA) and ultrasound (US) experimental set-up. (b) Matched filter algorithm used to generate A-scans;  $r(t)$ : reference signal (Chirp),  $s(t)$ : signal detected by the ultrasonic transducer, FFT and IFFT: fast Fourier transform and inverse FFT,  $Z^*$ : complex conjugate.



Data acquisition and signal processing were performed in the PC using LabView software. Linear frequency modulation chirps and a matched filtering method were employed to generate A-scans.<sup>46</sup> Figure 1(b) describes the signal generation pathway of matched filtering using the fast Fourier transform module (FFT). The cross-correlation (CC) signal was calculated by multiplying the Fourier transform of the detected signal with the complex conjugate of the Fourier transform of the reference signal. In addition to the in-phase CC, the quadrature CC was also calculated by eliminating the negative frequencies and making the signal analytic. In the end, the inverse FFT operator provided the CC in the time domain. Although the existence of real and imaginary parts generates a separate phase channel,<sup>50</sup> the phase signal was not used in this study because backscattering quantification was performed using integrated power spectrum. The chirp duration was 1 ms and A-scans were generated by averaging over 80 to 180 signal chirp records. The chirp bandwidth was adjusted to maximize the PA and US SNRs sequentially. In the PA (US) the frequency range used was 300 kHz to 2.6 MHz (300 kHz to 5 MHz).<sup>46</sup>

The employed laser power was 1.6 W and the beam spotsize after the collimator was 2 mm, which generates a fluence of 50 W/cm<sup>2</sup>. Despite the large fluence, its magnitude is under the maximum permissible exposure (MPE) due to the very short radiation time.<sup>49,51</sup> The chirps were transmitted in 10-ms batches, which correspond to MPE of 55 W/cm<sup>2</sup>. (MPE =  $1.1C_A t^{1/4}$  J/cm<sup>2</sup>,  $C_A = 1.58 \Rightarrow I = \text{MPE}/t = 55 \text{ W/cm}^2$ ).

The samples used in this work were goat rib bones (Canadian goat, Caprine). The samples were defatted by immersing in water for 3 weeks leading to natural soft tissue decomposition. Then, they were cleaned and washed and left to get completely dried. Also, a human trabecular bone (SteriGraft, San Antonio, Texas) from calcaneus was used for testing the cancellous bone alone. To perform decalcification simulating osteoporosis, 0.5-M ethylenediaminetetraacetic acid (EDTA) solution was used. This solution produces very slow and gentle demineralization and is extensively employed to simulate osteoporosis in bone tissue due to dissolving the bone minerals while leaving the organic components intact.<sup>52,53</sup> The extent of demineralization depends on solution concentration and exposure duration as well as exposed area and bone compactness. More details are given in Sec. 3.

### 3 Experimental Results and Discussion

#### 3.1 PA Response of a Cortical Layer

One experiment was introduced to demonstrate the possibility of detecting PA signals from below dense cortical layers. PA signals from a thin layer of goat cortical bone ( $1.5 \pm 0.06$  mm) between two adjacent locations were compared, such that in one case the underlayer was stained with graphite (Fig. 2). The strong peak due to the graphite layer indicated the penetration of laser light and the possibility of detecting PA signals below the cortical layer. Comparing the amplitude of the detected signal from cortical bone with the signal from the known sample, the bone absorption coefficient could be estimated. Bone absorption depends on bone compactness as well as concentration of the chromophores in the bone. Here, the frequency bandwidth is not in a range sensitive to the cortical bone porosity and therefore the response would be comparable to the signal from a flat surface with homogenous absorption. To extract the absorption coefficient, the photoacoustic induced pressure is normally approximated as<sup>54,55</sup>

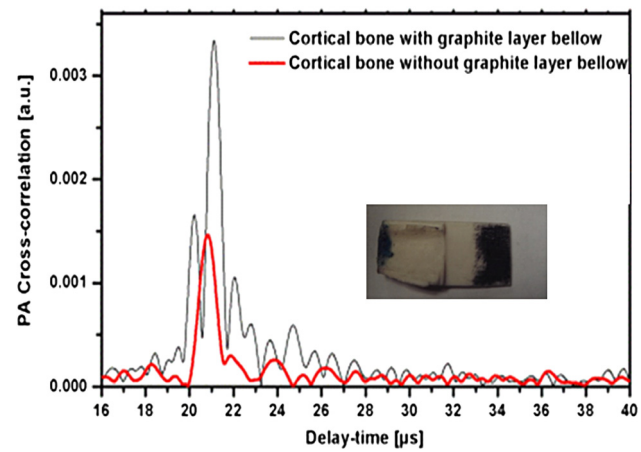


**Fig. 2** PA signal from a thin goat cortical bone ( $1.5 \pm 0.06$  mm) with and without graphite sublayer.

$$p_o \approx \Gamma \mu_a \Phi, \quad (5)$$

where  $\Gamma$  is the Grüneisen parameter,  $\mu_a$  is the absorption coefficient, and  $\Phi$  is the laser light fluence. This approximation is quite suitable for soft tissue, however due to large difference between the acoustic impedance of bone and coupling medium (water) proper approximation is<sup>46</sup>

$$p_o \propto \frac{\Gamma}{\left(1 + \frac{\rho_a c_a}{\rho_s c_s}\right)} \mu_a \Phi. \quad (6)$$

Here,  $c_a$  and  $c_s$  are the SOS in the bone and coupling medium (water), respectively, and  $\rho_a$  and  $\rho_s$  are the density of the bone and coupling medium, respectively. In this analysis, the thermal diffusion and shear waves in the bone are considered to be negligible and the SOS is in the perpendicular direction to the transducer. The value of the Grüneisen coefficient of cortical bones is considered to be 0.68 [with thermal expansion coefficient  $88 \times 10^{-6} \text{ K}^{-1}$  (Ref. 56), specific heat  $1.33 \text{ J} \cdot \text{g}^{-1} \cdot \text{K}^{-1}$  (Ref. 57), and SOS 3198 m/s; also the bone density is considered to be 1990 kg/m<sup>3</sup> (Ref. 58)]. We used a diluted solution of “Lamp Black” water color (Cotman Water Colours, Winsor & Newton, London, United Kingdom) as reference absorber. The absorption coefficient of the solution was measured optically by comparing the power of a CW laser passing through an empty 2-mm-glass spectrophotometer cell (cuvette) (Starna Cells Inc, Atascadero, California) and laser power passing through a cuvette filled with the solution. Using Beer’s law the absorption coefficient of the diluted water color was measured to be  $3.18 \text{ cm}^{-1}$ . The Grüneisen coefficient of diluted aqueous solution was estimated by the empirical formula;  $\Gamma = 0.0043 + 0.0053T$ , where  $T$  is the room temperature in deg Celsius. The PA measurement of water color solution was performed using a container with a very thin plastic surface on one side.<sup>49,59</sup> The cross-correlation amplitude is proportional to the detected pressure, thus, by comparing the peak amplitude of bones with the peak amplitude from the reference absorber and implementing the correction factor described in Eq. (6) we can estimate the absorption coefficient of bone. In this experiment, the laser power and all other parameters remain identical. This experiment yielded bone absorption coefficients between 0.08 and  $0.22 \text{ cm}^{-1}$  at 800-nm wavelength. These values are consistent with published literature values.<sup>47,60,61</sup>

### 3.2 PA and US Signals from a Human Trabecular Bone

In another experiment, PA and US backscattering signals from a trabecular bone block of human calcaneus were analyzed. The human bone lost its marrow and had reduced lipid elements following the cleaning procedure; however, the minerals were left intact. The size of the bone was  $15.7 \times 15.7 \times 35 \text{ mm}^3$ . Its apparent density was estimated to be  $360 \text{ mg/cm}^3$ , a value derived by weighing the bone and dividing the weight by its volume. On one side of the bone some holes were drilled, whereas the other side remained intact [Fig. 3(a)]. The distance from the holes to the tested surface was  $\sim 3 \text{ mm}$ . To eliminate the effect of the transducer and other instruments, the spectra of PA and US signals were normalized with reference signals conforming theoretically to Eqs. (1) and (2). An ideal reflecting material for US backscattering reference was a polished metal (here aluminum) surface, and for PA, a thick-homogeneous absorber (plastisol) with a known absorption coefficient of  $9 \text{ cm}^{-1}$ . The backscattered PA and US spectra from the abovementioned ideal reflector/absorber are shown in Fig. 3(b), where the ordinates are not to scale. A similar normalization procedure was performed for all our experiments.

The PA and US spectra were averaged over measurements at six points on the intact bone and six points over the holes. To make a comparison between the changes in the PA and US spectra, the centroids and spectral powers of US and PA signals in the same frequency range, 0.3 to 2.6 MHz, were considered. The spectral power is defined by the integrated power spectrum in Eq. (2), and the spectral centroid is defined as

Centroid frequency of PA/US spectrum

$$= \frac{1}{\Delta f} \int_{\Delta f} \left( \frac{S_r}{S_{\text{ref}}} \right) f df \text{ (Hz)}. \quad (7)$$

Figures 3(c) and 3(d) compare the averaged PA and US spectra for the two cases. There is no meaningful change between the spectra in the two cases compared with the signal variation from point to point. The integrated spectrum has been reduced by 5.1% and 3.7% over the hole for PA and US cases, respectively. The centroids of the PA spectra are  $1890 \pm 28$  ( $1918 \pm 23$ ) kHz for intact bone (over the hole), and  $1459 \pm 72$  ( $1724 \pm 63$ ) kHz for their US counterparts over the common frequency range 0.3 to 2.6 MHz. It can be seen that: (1) the centroid of the averaged spectrum has been increased by removing part of the trabecular bone below 3 mm for US and also PA (the change in PA centroid is statistically significant with 85% confidence based on *t*-test); (2) The change in the centroid is much smaller for the PA spectrum than for its US counterpart; and (3) the US centroid frequencies are lower than PA centroids. It should be mentioned that the PA low-pass effect has been accounted for after normalization with the homogeneous absorber, otherwise we would expect to have higher centroids for US spectra than for PA. The reason for the three above-mentioned observations can be attributed to ultrasonic attenuation in bone media, which increases with frequency and causes higher frequencies to be damped in the case of the intact bone compared with the drilled bone. US signals undergo greater high-frequency reduction than PA signals due to the double transmission path of the US backscattered signal.

Subsequently, in another experiment, the PA and US signals over the hole were compared with the signals after the hole was filled with a black rubber absorber (cylinder). This experiment

demonstrates that a laser-induced US signal can still be generated even below 3 mm of trabecular bone. Otherwise, the signals from this depth would be mostly attributed to the multiple scattering of US in the random scattering medium. The PA signals with and without the black rubber cylinder are compared in Fig. 3(e). It can be seen that by inserting the cylinder, a new peak appears in the corresponding depth with minimal changes to the first peak of the signal prior to the insertion. Figure 3(f) shows the US counterparts of the signals in Fig. 3(e). As shown, inserting the black rubber cylinder below 3 mm of trabecular layer has almost no effect on the US signal. This should be attributed to the large-acoustic attenuation of bone in the employed frequency range, note that due to echo measurements the attenuation depth is 6 mm in this case. The PA and US normalized power spectra in the same frequency range over the intact bone are compared in Figs 4(a)–4(c) for three different points. The PA and US spectra were normalized by use of the experimental signals from the perfect reflector/absorber as described above. The coherent backscattering effect can be detected in the presence of resonance peaks in both PA and US spectra. Coherent backscattering is considered as “unmistakable signature of multiple scattering”<sup>38</sup> and can be applied to estimate the scattering mean-free time in the bone, which corresponds to the distance between scatterers (trabeculae).<sup>38</sup> Therefore, we can expect to have similarities in the interfering frequencies of the two modalities. From the figures, we can see that PA generates more peaks because PA interferences are not only generated by coherent PA signals from trabeculae but also from their echoes: light reaches simultaneously all absorbing/PA signal generating targets which also respond simultaneously, thereby preserving their individual response character on a short (one-way) transit time scale to the transducer. The US excitation penetrates deeper than optical irradiation because the latter undergoes depth-dependent absorption attenuation, and it generates responses upon arrival at each target sequentially, which takes longer round-trip times. The US generated echoes from all layers with round-trip time delays add structure to the low-frequency end of the spectrum. The result is the PA- and US-generated spectra are heavily weighed at high and low frequencies, respectively, as seen in Fig. 3(b) and are, therefore, complementary. It is important to add that the attenuation of US signal from deeper layers is mainly a function of structural properties of the medium, whereas attenuation of the PA signal is a function of molecular composition in addition to the medium structure. In summary, in the combined US and PA signals both composition and structure are important factors in shaping the frequency spectra. Several similar structures appear in the mid-range of both spectra. For instance, the resemblance of peak and trough structure in the frequency range 1.5 to 2 MHz in Fig. 4(a) indicates that in both cases coherent backscattering is strongly correlated with the scattering mean-free time in the bone, which corresponds to trabecular thickness and separation. However, due to the frequency dependence of the PA signal phase, the phases at the peaks and troughs do not have a direct correspondence. The normalized PA spectrum specifically shows an increase with frequency, which is due to the distribution of trabeculae interdistances.

### 3.3 PA and US Signal Validation Using Microcomputed Tomography

In another experiment, the PA and US signals from a set of four defatted goat rib bones were analyzed with the goal to test PA

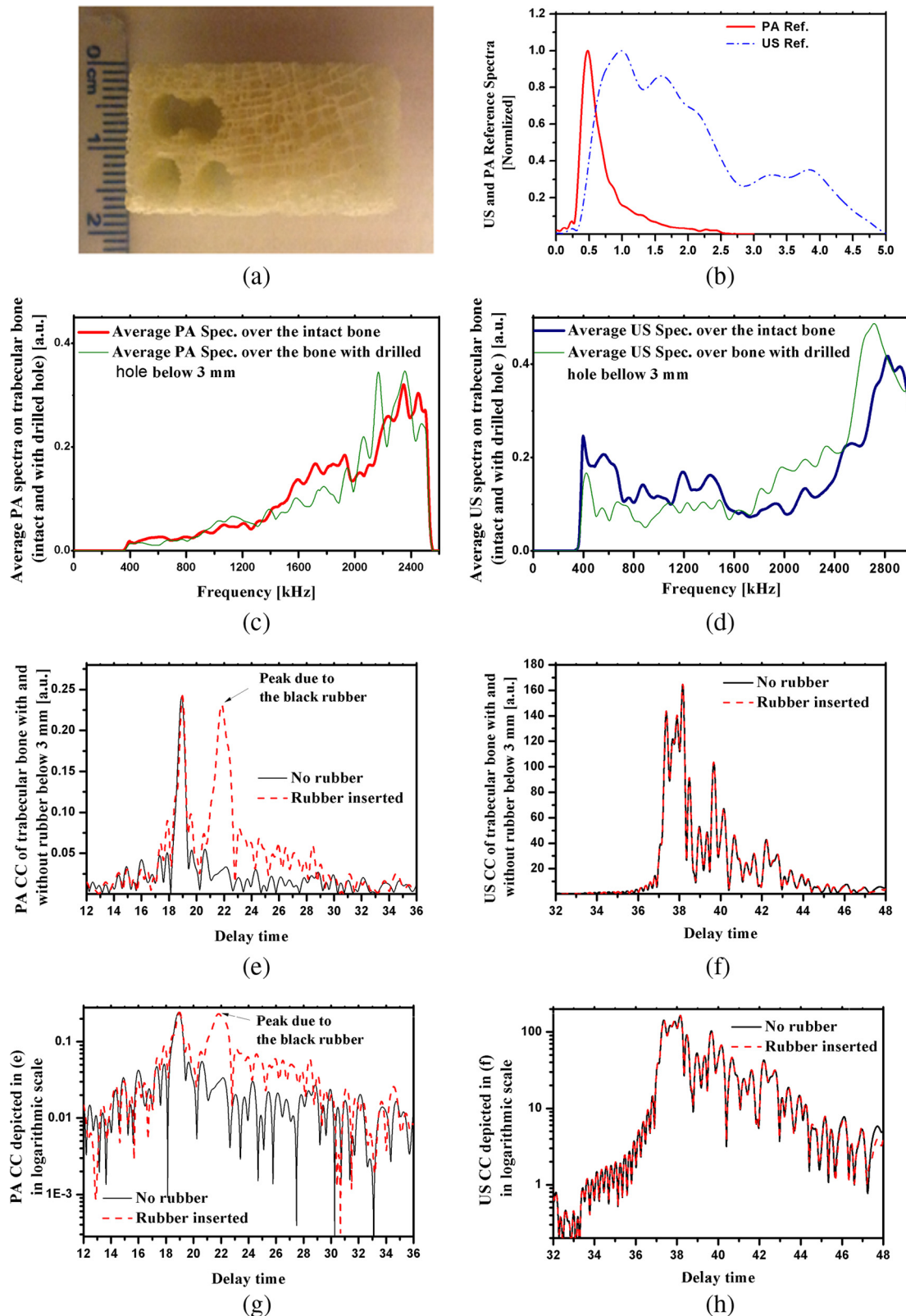


**Fig. 3** (a) Human trabecular bone sample. (b) Reference PA and US spectra used for respective normalizations. (c) Spatially averaged PA spectra (6 points) of trabecular intact bone and over the drilled region. (The average standard deviations divided by spectral amplitudes were 22% and 23%, respectively). (d) Spatially averaged US spectra (6 points) of trabecular intact bone and over the drilled region. (The average standard deviations divided by spectral amplitudes were 19% and 22%, respectively.) (e) PA cross-correlation envelope of trabecular bone over the drilled hole and after it was filled with black cylindrical rubber beneath 3 mm of cancellous bone. (f) US counterpart of (e) at the same point. (g) and (h) show the PA and US cross-correlations depicted in (e) and (f) in logarithmic scale respectively to highlight minor changes.



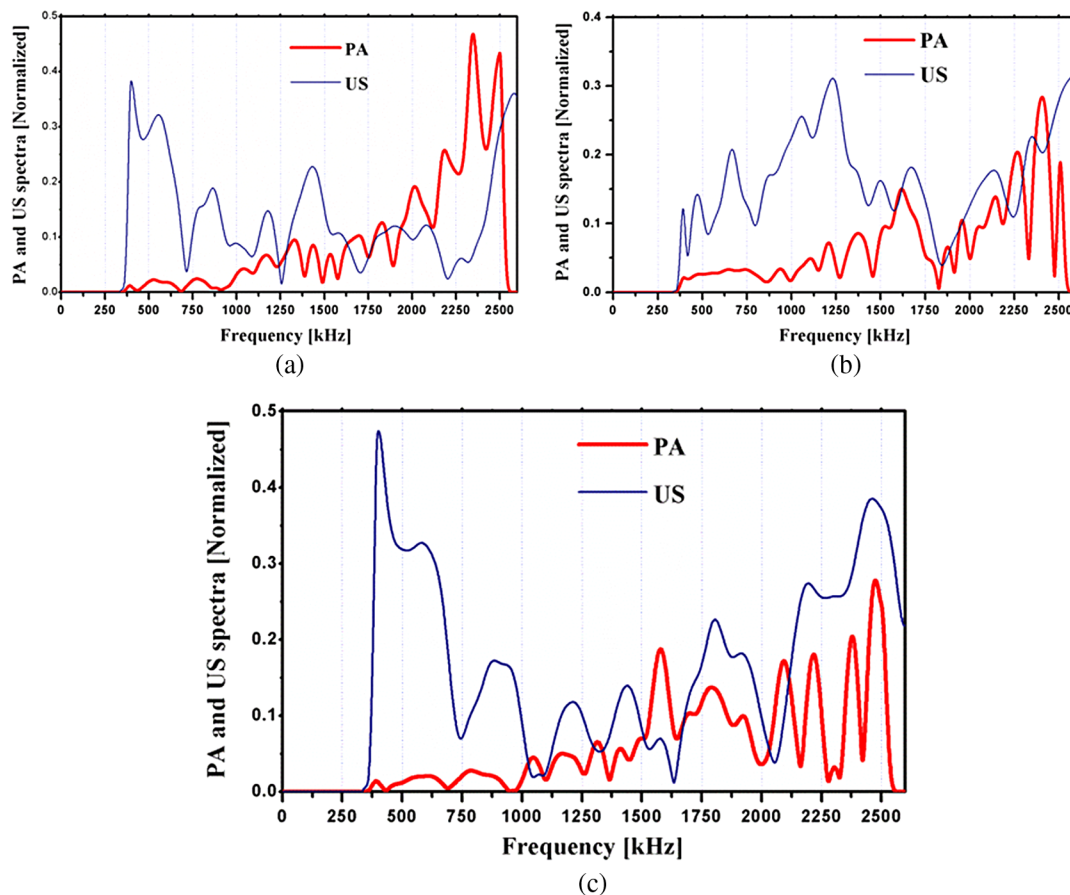


**Fig. 4** Comparison of PA and US spectra normalized with reference spectra for three different locations (a), (b), and (c) on the intact part of the cancellous bone in Fig. 3(a).

and US sensitivity to demineralization. As shown in Fig. 5(a) seven points with 1-mm distance between them were tested at different demineralization stages. The demineralization solution was made by diluting 50 ml of EDTA solution (0.5 M, pH = 8) in equal volume of distilled water, which generates a pH of 7.7. The EDTA solution produces very slow and gentle decalcification and its mild solution (pH  $\leq 8$ ) has been widely used in the literature for simulating artificial osteoporosis.<sup>52,53,62</sup> The four bone samples were kept in the solution for 10, 20, 30, and 40 h of demineralization, respectively. The samples were attached to Lego blocks to ensure the tests had been performed at the same locations on the ribs before and after demineralization. The fourth sample was demineralized without removal of the bone, to ensure successive measurements from exactly the same points. To validate the US and PA results with an established method of BMD assessment, the samples were also imaged with microcomputed tomography ( $\mu$ CT). The  $\mu$ CT scans were performed in the air using a SkyScan system (SkyScan, Belgium) with the settings: 60 kV, 167  $\mu$ A, 0.25 step size, four frame average,  $4000 \times 2672$  pixel matrix, and a  $5\text{-}\mu\text{m}^2$  pixel size. Total scan time was 2.5 h. Images were reconstructed using a modified Feldkamp cone-beam algorithm.<sup>63</sup> Subsets of the data were created which included all bone parts within the rib and spanned the region between the two arrows in Fig. 5(a). That section consists of 760  $\mu$ CT slices. Three analysis regions were determined on the rib sample: middle region of the dorsal cortical shell, trabecular bone of the rib, and both of these tissues together. The  $\mu$ CT slices of

the fourth sample in three directions are shown before demineralization, Fig. 5(b), and after 40 h of demineralization, Fig. 5(c). The ensemble-averaged PA and US cross-correlation signals of the fourth sample are shown in Figs. 5(d) and 5(e), respectively. These signals show the variation of averaged US and PA signals from cortical and trabecular layers of intact and 40-h demineralized bone. It can be observed that the variation of the reflected US signal from the cortical layer is minor, while the first peak of PA signal changed significantly. On the other hand, in the deeper layers the PA signal increased with demineralization. This can be explained by considering that demineralization reduces optical scattering and thus may allow optical energy to access deeper layers more effectively.

Time gating has allowed separation of the reflected US and back-propagated PA signals from the cortical layer. The spectra of these signals were normalized with the respective reference spectra similar to the previous experiment. Integrating over the frequency range, the US IRC and PA AIB from the cortical layer were calculated [Eq. (2)]. Likewise, by time gating the cortical- and trabecular-backscattered signals together, the total integrated US and PA backscattering coefficients can be calculated. Variations of the integrated backscattered signals versus BMD of the cortical and the combined cortical and trabecular volume of interest derived from  $\mu$ CT are shown in Figs. 6(a) and 6(b). For the third sample, the extent of trabecular demineralization was too high after 30 h and therefore this sample was excluded from the total cortical and trabecular result statistics after demineralization. The trabecular region of the fourth sample was less

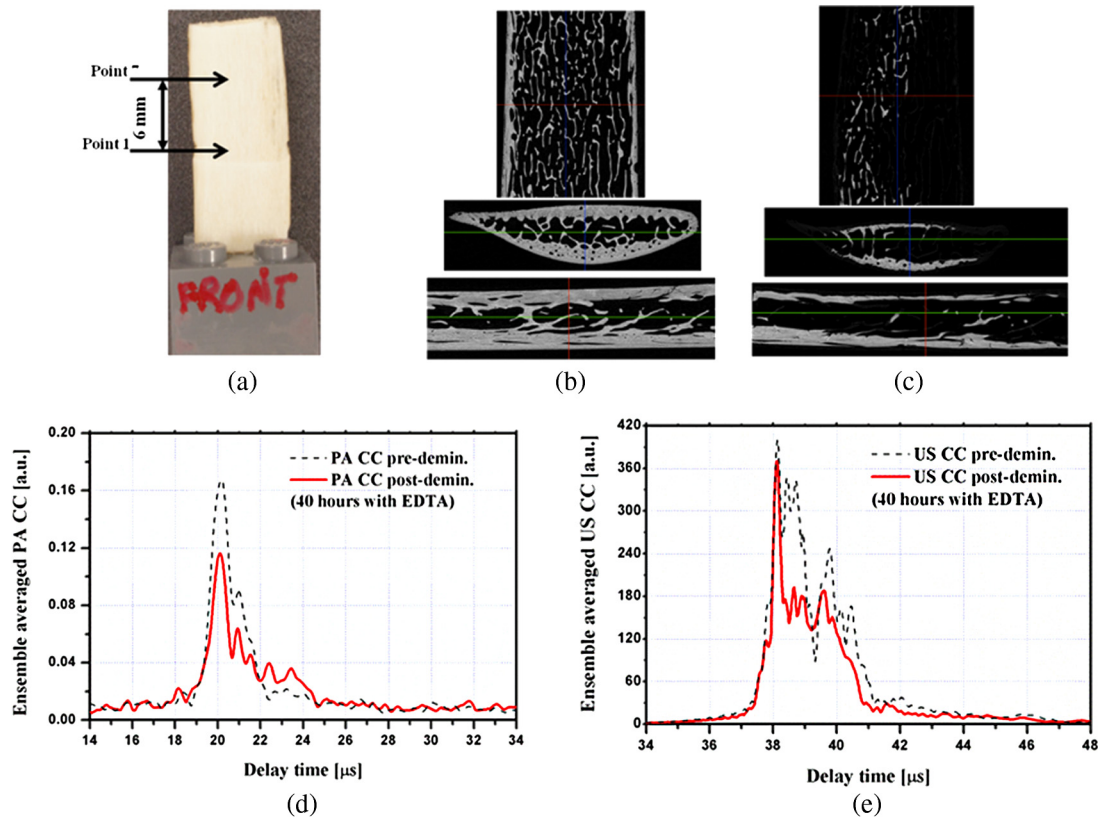


**Fig. 5** (a) A goat rib sample with measurement region, points 1 to 7, shown between arrows. Three  $\mu$ CT slice images of the goat bone in three orientations: (b) before and (c) after 40-h demineralization with EDTA solution. The ensemble averaged over the 7 points (d) PA and (e) US envelope cross-correlation signals before and after 40-h demineralization.

demineralized compared with the third sample despite the fact that they were demineralized for 40 and 30 h, respectively. The main difference between the demineralization process of the fourth sample and that of the others was that this rib bone was located horizontally in the demineralization tank while other samples were hung in the solution. The linear regressions of the measurements show the degree of correlation and sensitivity of PA and US to changes in bone density in the cortical

and cancellous regions. Comparison of the slope of the lines demonstrates the higher sensitivity of PA to BMD variations in the cortical part. As seen in the figures, the variances are quite large which is due to the nature of the experiment and variability and inhomogeneity of real bone tissue, rather than the result of low SNRs. Figures 7(a) and 7(b) compare the point-by-point variation of US and PA backscatter from cortical layers of the first and second sample before and after 10 and 20 h of

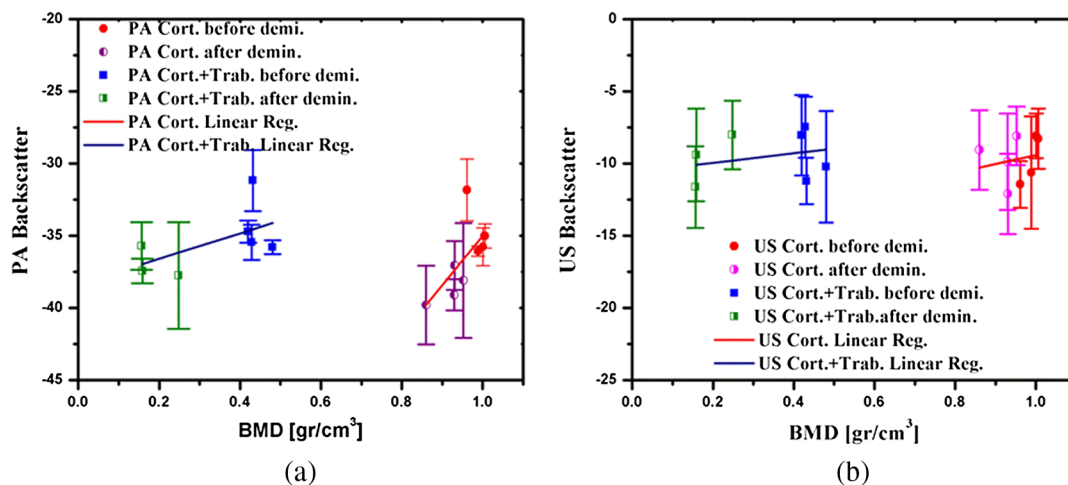


**Fig. 6** The integrated (a) PA and (b) US-backscattered signals of cortical and combined cortical and trabecular bone versus BMD of volume of interest as obtained from  $\mu$ CT analysis.



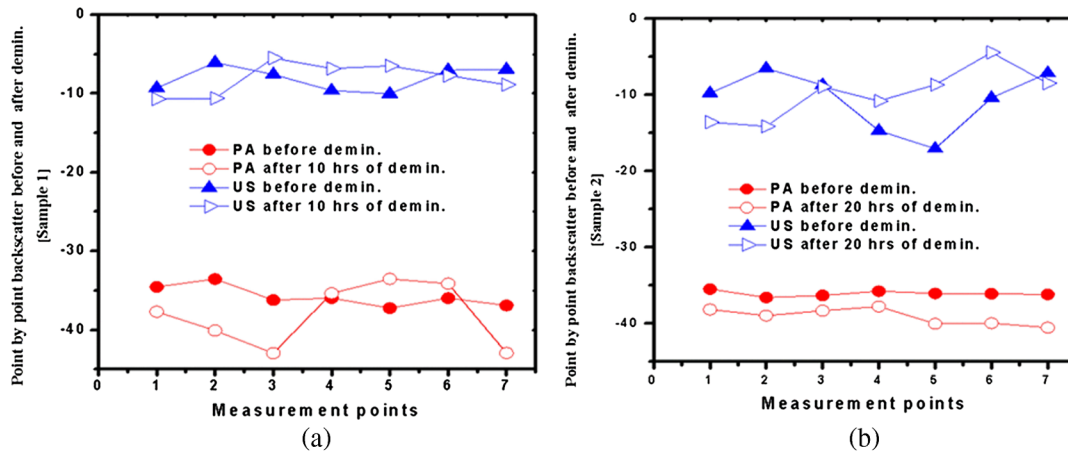


**Fig. 7** Point by point US and PA-backscattered signal variations from samples (a) 1 and (b) 2, before and after 10- and 20-h demineralization, respectively.

**Table 1** Changes of integrated photoacoustic (PA) and ultrasound (US) backscatter parameters due to bone demineralization (artificial osteoporosis).

Sample	Hours of demin.	Bone mineral density (BMD) before demin.	BMD after demin.	PA change of cortical back propagation (dB)	US change of cortical back reflection (dB)
#1	10	1.001	0.953	2.33	0.01
#2	20	0.988	0.930	3.04 <sup>a</sup>	-0.75
#3	30	1.005	0.860	4.79 <sup>a</sup>	0.76
#4	40	0.961	0.931	5.23 <sup>a</sup>	0.65

<sup>a</sup>Statistically significant with 90% confidence.

demineralization, respectively. The comparison between the point-by-point changes and variations due to demineralization demonstrate the main challenge of assessment of biological tissue. The sensitivity of each modality should be able to dominate the natural variation of properties in the tissue and yield meaningful statistical analysis. Strictly speaking, this is achieved only with the PA signal after 20 h of demineralization. Using a statistical *t*-test for the results, the majority of the integrated PA-backscattered measurements demonstrates statistically significant reduction with 90% confidence. Table 1 shows the changes of BMD and integrated PA back-propagation and US reflection from the cortical layer. Except the first sample after 10 h of demineralization, in all other PA cases, the changes were significant while none of the US results show adequate sensitivity to BMD variation in the cortical layer.

The variation of US IRC and PA AIB (cortical layer only) of eight samples versus hours of demineralization is shown in Fig. 8. The four cortical samples were the same ones described before (rib cortical) and another four measurements were performed from the other side of the same samples. The signal variation was larger across the opposite sides of the ribs compared with different locations on the same side. Figure 8 demonstrate that the average change of PA AIB in the cortical layer is significantly larger than the standard deviation of the properties at each stage, while this is not the case with US IRC (cortical

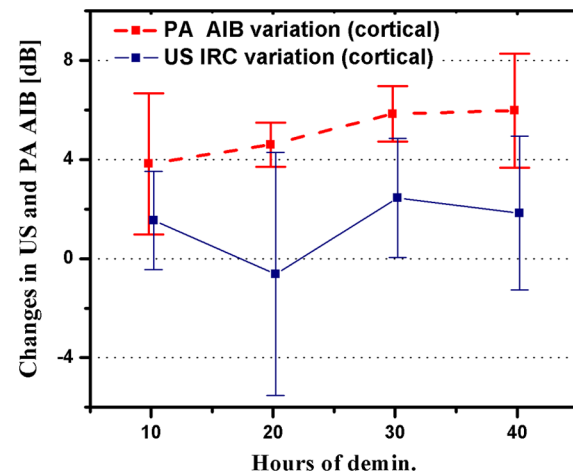


**Fig. 8** The variation of PA and US-backscattered signal from the cortical layer (in US it is the reflection parameter IRC) versus hours of demineralization.

layer). Hence, Fig. 8 is consistent with the statistical analysis described in Table 1, over a larger set of samples.

## 4 Conclusions

Among the QUS challenges are the large variability of properties in biological tissue and the large number of material parameters in contrast with the limited measurable parameters. The former issue is also relevant to DXA; for instance, changing the skeletal test site can substantially change the number of designated osteoporosis patients in a given population.<sup>64</sup> In clinical applications, use of collected demographic information as a complementary source may help in bone loss assessments but cannot compensate for these deficiencies. The ultimate goal of this study was to add to the number of measurable parameters by simultaneous measurement of PA- and US-backscattered signals. Combining PA and US methods and their different sensitivities to transmission and backscattered modes provides the benefit of better understanding the acoustic attenuation mechanism in cancellous bone and the contribution of absorption and scattering in different frequency ranges.<sup>13,65</sup>

This study shows that it is possible to detect PA signals *in-vitro* from below a thin layer of cortical bone as well as below

a few millimeters of the trabecular bone [Figs. 2 and 3(e)]. Although PA can reach several centimeters beneath the surface of soft tissue, the higher optical scattering and acoustic attenuation in bone limit PA penetration in deep hard tissue. Measurements on a trabecular human bone show that coherent backscattering can affect PA signals in a manner similar to US. Although the PA spectrum exhibits more resonance frequencies or constructive interferences, there are similar resonance frequencies in PA and US spectra [Figs. 4(a)–4(c)]. These coherent backscatter frequencies can be employed to estimate the TrSp distance.

Osteoporotic changes in the bone were simulated by using a very mild demineralization (EDTA) solution. Changes in the cross-correlation signals were compared for each sample after demineralization. Results showed the ability of US to generate detectable signals from deeper bone sublayers, whereas the PA signals show higher sensitivity to cortical bone density variations. Although US signal variation with changes in the cortical layer is insignificant, PA was able to detect even minor variations in the cortical bone density. Although the effect of osteoporosis on the cortical layer is approximately eight times slower than the trabecular layer,<sup>66</sup> the higher sensitivity of the PA technique can provide a valuable noninvasive monitor of osteoporosis on bone surfaces without the need to penetrate the deeper underlying trabecular structure. It is interesting to note that some studies suggest that osteoporosis changes in the bone have correlation even with fingernail composition.<sup>67,68</sup> In the subsequent work, we study the PA and US backscattering in trabecular samples, and we show that PA is not only sensitive to mineral density variation but also to collagen content. On the other hand, US backscattering is mainly sensitive to BMD variation.

In conclusion, the coregistration of US- and PA-backscattered signals provides a versatile method capable of better assessment of bone health and may become a viable technique for *in-vivo* noninvasive monitoring of osteoporosis in load-bearing bones (spine, femur).

## Acknowledgments

The authors gratefully acknowledge the support of the Canada Council for the Arts through a Killam Fellowship to A.M. The guidance and recommendations of Dr. M. D. Grynpas and Dr. T. L. Willett from Samuel Lunenfeld Research Institute, Mount Sinai Hospital are greatly appreciated. They also acknowledge the help of Dr. B. T. Amaechi and Mr. J. Schmitz (University of Texas, Health Science Center at San Antonio) for performing #956/CT procedures and of Dr. J. E. Davis (IBBME, University of Toronto) for providing the human bone sample.

## References

1. B. C. Silva and J. P. Bilezikian, "New approaches to the treatment of osteoporosis," *Annu. Rev. Med.* **62**, 307–322 (2011).
2. I. Fogelman and G. M. Blake, "Different approaches to bone densitometry," *J. Nucl. Med.* **41**(12), 2015–2025 (2000).
3. B. Häussler et al., "Epidemiology, treatment and costs of osteoporosis in Germany—the BoneEVA study," *Osteoporos. Int.* **18**(1), 77–84 (2007).
4. P. Laugier and G. Häfät, *Bone Quantitative Ultrasound*, Springer, Dordrecht, Netherlands (2011).
5. J.-E. Tarride et al., "The burden of illness of osteoporosis in Canadian men," *J. Bone Miner. Res.* **27**(8), 1830–1838 (2012).
6. P. Augat and F. Eckstein, "Quantitative imaging of musculoskeletal tissue," *Annu. Rev. Biomed. Eng.* **10**, 369–390 (2008).

7. C. M. Langton and C. F. Njeh, "The measurement of broadband ultrasonic attenuation in cancellous bone—a review of the science and technology," *IEEE Trans. Ultrason. Ferroelect. Freq. Contr.* **55**(7), 1546–1554 (2008).
8. P. Laugier, "Instrumentation for *in vivo* ultrasonic characterization of bone strength," *IEEE Trans. Ultrason. Ferroelect. Freq. Contr.* **55**(6), 1179–1196 (2008).
9. D. Hans and M.-A. Krieg, "The clinical use of quantitative ultrasound (QUS) in the detection and management of osteoporosis," *IEEE Trans. Ultrason. Ferroelect. Freq. Contr.* **55**(7), 1529–1538 (2008).
10. K. Wear, "Ultrasonic scattering from cancellous bone: a review," *IEEE Trans. Ultrason. Ferroelect. Freq. Control* **55**(7), 1432–1441 (2008).
11. F. Jensen et al., "In vitro ultrasonic characterization of human cancellous femoral bone using transmission and backscatter measurements relationships to bone mineral density," *J. Acoust. Soc. Am.* **119**(1), 654–663 (2006).
12. S. Chaffai et al., "Ultrasonic characterization of human cancellous bone using transmission and backscatter measurements relationships to density and microstructure," *Bone* **30**(1), 229–237 (2002).
13. B. Hoffmeister, "Frequency dependence of apparent ultrasonic backscatter from human cancellous bone," *Phys. Med. Biol.* **56**(3), 667–683 (2011).
14. S. Chaffai et al., "Frequency dependence of ultrasonic backscattering in cancellous bone: autocorrelation model and experimental results," *J. Acoust. Soc. Am.* **108**(5), 2403–2411 (2000).
15. K. W. Wear and B. S. Garra, "Assessment of bone density using ultrasonic backscatter," *Ultrasound Med. Biol.* **24**(5), 689–695 (1998).
16. D. Ta et al., "Analysis of frequency dependence of ultrasonic backscatter coefficient in cancellous bone," *J. Acoust. Soc. Am.* **124**(6), 4083–4090 (2008).
17. K. I. Lee and M. J. Choi, "Frequency-dependent attenuation and backscatter coefficients in bovine trabecular bone from 0.2 to 1.2 MHz," *J. Acoust. Soc. Am.* **131**(1), EL67–EL73 (2012).
18. F. Jensen et al., "In vitro ultrasonic characterization of human cancellous femoral bone using transmission and backscatter measurements: relationships to bone mineral density," *J. Acoust. Soc. Am.* **119**(1), 654–663 (2006).
19. K. Wear, "Frequency dependence of ultrasonic backscatter from human trabecular bone theory and experiment," *J. Acoust. Soc. Am.* **106**(6), 3659–3664 (1999).
20. K. Wear, "Measurement of dependence of backscatter coefficient from cylinders on frequency and diameter using focused transducers—with applications in trabecular bone," *J. Acoust. Soc. Am.* **115**(1), 66–72 (2004).
21. M. A. Hakulinen et al., "Ability of ultrasound backscattering to predict mechanical properties of bovine trabecular bone," *Ultrasound Med. Biol.* **30**(7), 919–927 (2004).
22. O. Riekkinen et al., "Spatial variation of acoustic properties is related with mechanical properties of trabecular bone," *Phys. Med. Biol.* **52**(23), 6961–6968 (2007).
23. J. P. Karjalainen et al., "Ultrasound backscatter imaging provides frequency-dependent information on structure, composition and mechanical properties of human trabecular bone," *Ultrasound Med. Biol.* **35**(8), 1376–1384 (2009).
24. B. K. Hoffmeister et al., "Ultrasonic characterization of cancellous bone using apparent integrated backscatter," *Phys. Med. Biol.* **51**(11), 2715–2727 (2006).
25. B. K. Hoffmeister et al., "Ultrasonic characterization of human cancellous bone in vitro using three different apparent backscatter parameters in the frequency range 0.6–15 MHz," *IEEE Trans. Ultrason. Ferroelect. Freq. Control* **55**(7), 1442–1452 (2008).
26. O. Riekkinen et al., "Acoustic properties of trabecular bone relationships to tissue composition," *Ultrasound Med. Biol.* **33**(9), 1438–1444 (2007).
27. F. Padilla et al., "Relationships of trabecular bone structure with quantitative ultrasound parameters: in vitro study on human proximal femur using transmission and backscatter measurements," *Bone* **42**(6), 1193–1202 (2008).
28. K. Wear, "Characterization of trabecular bone using the backscattered spectral centroid shift," *IEEE Trans. Ultrason. Ferroelect. Freq. Control* **50**(4), 402–407 (2003).

29. F. Jenson, F. Padilla, and P. Laugier, "Prediction of frequency-dependent ultrasonic backscatter in cancellous bone using statistical weak scattering model," *Ultrasound Med. Biol.* **29**(3), 455–464 (2003).
30. O. Riekkinen et al., "Dual frequency ultrasound new pulse echo technique for bone densitometry," *Ultrasound Med. Biol.* **34**(10), 1703–1708 (2008).
31. J. Karjalainen et al., "Dual-frequency ultrasound technique minimizes errors induced by soft tissue in ultrasound bone densitometry," *Acta Radiol.* **49**(9), 1038–1041 (2008).
32. P. Moilanen, "Ultrasonic guided waves in bone," *IEEE Trans. Ultrason. Ferroelect. Freq. Contr.* **55**(6), 1277–1286 (2008).
33. P. A. Lomei Mejia et al., "Photoacoustic spectroscopy applied to the study of bone consolidation in fractures," *Mater. Sci. Forum* **480–481**, 339–344 (2005).
34. T. Li and R. J. Dewhurst, "Photoacoustic imaging in both soft and hard biological tissue," *J. Phys.: Conf. Ser. (ICPP15)* **214**, 012028 (2010).
35. X. Wang, D. L. Chamberland, and D. A. Jamadar, "Noninvasive photoacoustic tomography of human peripheral joints toward diagnosis of inflammatory arthritis," *Opt. Lett.* **32**(20), 3002–3004 (2007).
36. G. Xu et al., "PA and US dual modality imaging of human peripheral joints," *J. Biomed. Opt.* **18**(1), 010502 (2013).
37. B. Lashkari and A. Mandelis, "Combined photoacoustic and ultrasonic diagnosis of early bone loss and density variations," *Proc. SPIE* **8207**, 82076K (2012).
38. A. Derode et al., "Dynamic coherent backscattering in a heterogeneous absorbing medium: application to human trabecular bone characterization," *Appl. Phys. Lett.* **87**(11), 114101 (2005).
39. Z. Zhao et al., "Photo-acoustic excitation and detection of guided ultrasonic waves in bone samples covered by a soft coating layer," *Proc. SPIE* **8553**, 85531E (2012).
40. I. Steinberg, A. Eyal, and I. Gannot, "Multispectral photoacoustic method for the early detection and diagnosis of osteoporosis," *Proc. SPIE* **8565**, 85656G (2013).
41. A. Nowicki et al., "Estimation of ultrasonic attenuation in a bone using coded excitation," *Ultrasonics* **41**(8), 615–621 (2003).
42. W. Lin, Y. Xia, and Y. X. Qin, "Characterization of the trabecular bone structure using frequency modulated ultrasound pulse," *J. Acoust. Soc. Am.* **125**(6), 4071–4077 (2009).
43. B. Lashkari et al., "Slow and fast ultrasonic wave detection improvement in human trabecular bones using Golay code modulation," *J. Acoust. Soc. Am.* **132**(3), EL222–EL228 (2012).
44. X. Song, D. Ta, and W. Wang, "A base-sequence-modulated Golay code improves the excitation and measurement of ultrasonic guided waves in long bones," *IEEE Trans. Ultrason. Ferroelect. Freq. Control* **59**(11), 2580–2583 (2012).
45. T. Misaridis and J. A. Jensen, "Use of modulated excitation signals in medical ultrasound, part II: design and performance for medical imaging applications," *IEEE Trans. Ultrason. Ferroelect. Freq. Control* **52**(2), 192–207 (2005).
46. B. Lashkari and A. Mandelis, "Linear frequency modulation photoacoustic radar: optimal bandwidth for frequency-domain imaging of turbid media," *J. Acoust. Soc. Am.* **130**(3), 1313–1324 (2011).
47. E. A. Genina, A. N. Bashkatov, and V. V. Tuchin, "Optical clearing of cranial bone," *Adv. Opt. Technol.* **2008**, 267867 (2008).
48. "Panametrics—NDT ultrasonic transducers for nondestructive testing," Pana\_UT\_EN\_201301, Olympus NDT, p. 43, 2011, <http://www.olympus-ims.com/en/ultrasonic-transducers/> (6 March 2014).
49. B. Lashkari and A. Mandelis, "Comparison between pulsed laser and frequency-domain photoacoustic modalities: signal-to-noise ratio, contrast, resolution, and maximum depth detectivity," *Rev. Sci. Instrum.* **82**(9), 094903 (2011).
50. B. Lashkari and A. Mandelis, "Photoacoustic radar imaging; signal-to-noise ratio, contrast, and resolution enhancement using nonlinear chirp modulation," *Opt. Lett.* **35**(10), 1623–1625 (2010).
51. American National Standards Institute, "American national standard for the safe use of lasers," Standard Z136.1-2007, ANSI Inc., New York (2007).
52. G. Callis and D. Sterchi, "Decalcification of bone literature review and practical study of various decalcifying agents methods and their effect on bone histology," *J. Histotechnol.* **21**(1), 49–58 (1998).
53. H. Ehrlich et al., "Principles of demineralization modern strategies for the isolation of organic frameworks, part II decalcification," *Micron* **40**(2), 169–193 (2009).
54. A. A. Oraevsky, S. L. Jacques, and F. K. Tittel, "Measurement of tissue optical properties by time-resolved detection of laser-induced transient stress," *Appl. Opt.* **36**(1), 402–415 (1997).
55. B. Cox et al., "Quantitative spectroscopic photoacoustic imaging: a review," *J. Biomed. Opt.* **17**(6), 061202 (2012).
56. S. B. Lang, "Thermal expansion coefficients and the primary and secondary pyroelectric coefficients of animal bone," *Nature* **224**, 798–799 (1969).
57. F. Duck, *Physical Properties of Tissue: A Comprehensive Review*, Academic Press, London (1990).
58. T. L. Szabo, *Diagnostic Ultrasound Imaging: Inside Out*, Elsevier Academic Press, Burlington (2004).
59. S. A. Telenkov and A. Mandelis, "Photothermoacoustic imaging of biological tissues: maximum depth characterization comparison of time and frequency-domain measurements," *J. Biomed. Opt.* **14**(4), 044025 (2009).
60. A. Pifferi et al., "Optical biopsy of bone tissue: a step toward the diagnosis of bone pathologies," *J. Biomed. Opt.* **9**(3), 474–480 (2004).
61. A. N. Bashkatov et al., "Optical properties of human cranial bone in the spectral range from 800 to 2000 nm," *Proc. SPIE* **6163**, 616310 (2006).
62. B. K. Hoffmeister et al., "Effect of collagen content and mineral content on the high-frequency ultrasonic properties of human cancellous bone," *Osteoporosis Int.* **13**, 26–32 (2002).
63. L. A. Feldkamp, L. C. Davis, and J. W. Kress, "Practical cone-beam algorithm," *J. Opt. Soc. Am.* **1**(6), 612–619 (1984).
64. M. L. Frost, G. M. Blake, and I. Fogelman, "Can the WHO criteria for diagnosing osteoporosis be applied to calcaneal quantitative ultrasound?," *Osteoporosis Int.* **11**(4), 321–330 (2000).
65. C. Roux et al., "Ultrasonic backscatter and transmission parameters at the os calcis in postmenopausal osteoporosis," *J. Bone Miner. Res.* **16**(7), 1353–1362 (2001).
66. C. Langton, "Osteoporosis: case of skeletal biocorrosion," *Corros. Eng. Sci. Technol.* **42**(4), 339–343 (2007).
67. I. Pillay et al., "The use of fingernails as a means of assessing bone health: a pilot study," *J. Women's Health* **14**(4), 339–344 (2005).
68. A. Hossein-nezhad et al., "The fingernail protein content may predict bone turnover in postmenopausal women," *Iranian J. Publ. Health. (A supplementary issue on Osteoporosis and Bone Turnover)* **37**, 55–62 (2008).

**Bahman Lashkari** is a postdoctoral fellow at the Center for Advanced Diffusion-Wave Technologies, where he works on several photoacoustic and ultrasound projects. He conducted his PhD in the same lab, working on frequency-domain photoacoustic imaging (2011). His research interests are in medical imaging and tissue characterization.

**Andreas Mandelis** is a full professor of mechanical and industrial engineering; electrical and computer engineering; and the Institute of Biomaterials and Biomedical Engineering, University of Toronto. He is the director of the Center for Advanced Diffusion-Wave Technologies. He is the author and co-author of more than 330 scientific papers in refereed journals and 180 scientific and technical proceedings papers. He is an editor of the *Journal of Biomedical Optics*, *Journal of Applied Physics*, *International Journal of Thermophysics*, and *Optics Letters*.